



HAL
open science

327 Gbps THz silicon photonic interconnect with sub- λ bends

Manoj Gupta, Nikhil Navaratna, Pascal Szriftgiser, Guillaume Ducournau,
Ranjan Singh

► **To cite this version:**

Manoj Gupta, Nikhil Navaratna, Pascal Szriftgiser, Guillaume Ducournau, Ranjan Singh. 327 Gbps THz silicon photonic interconnect with sub- λ bends. Applied Physics Letters, 2023, 123 (17), 10.1063/5.0168016 . hal-04272193

HAL Id: hal-04272193

<https://hal.science/hal-04272193v1>

Submitted on 23 Dec 2024

HAL is a multi-disciplinary open access archive for the deposit and dissemination of scientific research documents, whether they are published or not. The documents may come from teaching and research institutions in France or abroad, or from public or private research centers.




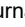


L'archive ouverte pluridisciplinaire **HAL**, est destinée au dépôt et à la diffusion de documents scientifiques de niveau recherche, publiés ou non, émanant des établissements d'enseignement et de recherche français ou étrangers, des laboratoires publics ou privés.



Distributed under a Creative Commons Attribution 4.0 International License

RESEARCH ARTICLE | OCTOBER 23 2023

327 Gbps THz silicon photonic interconnect with sub- λ bends

Manoj Gupta ; Nikhil Navaratna ; Pascal Szriftgiser ; Guillaume Ducournau ; Ranjan Singh  



Appl. Phys. Lett. 123, 171102 (2023)

<https://doi.org/10.1063/5.0168016>



Articles You May Be Interested In

Photonic THz mixers based on iron-doped InGaAs embedded in a plasmonic microcavity

APL Photonics (November 2023)

High-bandwidth density silicon photonic resonators for energy-efficient optical interconnects

Appl. Phys. Rev. (November 2023)

Selecting alternative metals for advanced interconnects

J. Appl. Phys. (November 2024)



Applied Physics Letters

Special Topics Open
for Submissions

[Learn More](#)

327 Gbps THz silicon photonic interconnect with sub- λ bends

Cite as: Appl. Phys. Lett. **123**, 171102 (2023); doi: [10.1063/5.0168016](https://doi.org/10.1063/5.0168016)

Submitted: 17 July 2023 · Accepted: 6 October 2023 ·

Published Online: 23 October 2023



View Online



Export Citation



CrossMark

Manoj Gupta,^{1,2}  Nikhil Navaratna,^{1,2}  Pascal Szriftgiser,³  Guillaume Ducournau,⁴  and Ranjan Singh^{1,2,a)} 

AFFILIATIONS

¹Division of Physics and Applied Physics, School of Physical and Mathematical Sciences, Nanyang Technological University, Singapore 637371, Singapore

²Center for Disruptive Photonic Technologies, The Photonics Institute, Nanyang Technological University, Singapore 639798, Singapore

³Laboratoire de Physique des Lasers, Atomes et Molécules, PhLAM, UMR 8523, Université de Lille, CNRS, 59655 Villeneuve d'Ascq, France

⁴Université de Lille, CNRS, Centrale Lille, University Polytechnique Hauts-de-France, UMR 8520, IEMN—Institut d'Electronique de Microélectronique et de Nanotechnologie, Lille, France

^{a)}Author to whom correspondence should be addressed: ranjans@ntu.edu.sg

ABSTRACT

Miniaturized photonic devices at the terahertz (THz) band are envisioned to bring significant enhancement to data transfer capacity and integration density for computing and future wireless communications. Broadband silicon waveguiding technology has continuously matured to advance low-loss platforms for integrated solutions. However, challenges are faced in realizing compact waveguiding platforms with different degrees of bends due to bend induced losses and mode distortion. Here, we demonstrate multiple bend incorporated photonic crystal waveguide platforms for multicarrier on-chip transmission. Our silicon interconnect device exhibits optimized bending radius to the free space wavelength ratio of 0.74, without signal distortion and transmission bandwidth of 90 GHz, representing 25.4% fractional bandwidth at 355 GHz. The broadband waveguide interconnect enables an aggregate data transfer rate of 327 Gbps by sending the complex modulated data over multiple carriers. This work augments the development of THz photonic integrated circuit for the future generations of on-chip high data rate interconnect and wireless communication, ranging from the sixth to X generation (6G to XG).

Published under an exclusive license by AIP Publishing. <https://doi.org/10.1063/5.0168016>

The ever-increasing demand for higher bandwidths and data rates mandates a move to the higher carrier frequencies enabled by the Terahertz (THz) frequency region.¹ The next generation of integrated technology will be based in the frequencies between 0.1 and 10 THz where bandwidths exceeding tens of GHz are possible.^{2,3} Consequently, by Shannon's theorem, higher channel capacities and data rates are achievable in this frequency region. The move to THz frequencies is also catalyzed by desirable traits of these frequencies like non-ionizing radiation and the presence of spectral features that enable a myriad of applications ranging from THz spectroscopy,⁴ sensing,^{5,6} imaging,^{7,8} high-resolution radar,⁹ and wave trapping.¹⁰ The lower losses and straightforward integration with conventional CMOS technology make on-chip silicon (Si) waveguides a key platform to fully harness the advantages accrued in the THz frequencies.¹¹ In addition to these advantages, the control of electromagnetic (EM) mode propagation by planar components starkly contrasts with metallic THz

waveguides whose bulkiness, high insertion, and Ohmic losses complicate their integration in THz systems.¹² Looking toward THz-ICs for 6G to XG, the next generation of communication systems will require devices and sub-systems where denser integration and higher bandwidths are possible.^{13–15} While bending of propagation channels reduces the chip footprint and facilitates the interconnection of multiple functionalized components, higher bandwidths boost the transport of data through multiple channels across different frequency bands on a single miniaturized chip.

Photonic crystal (PC) slabs present a convenient way to design high bandwidth Si THz waveguides.¹⁶ They are two-dimensional structures made with dielectric materials featuring perforated air holes. Arrays of such perforated air holes create a periodically varying refractive index in the structure leading to a photonic bandgap (PBG) where no electromagnetic modes exist.¹⁷ Compact THz waveguides can be made by introducing a line defect. This is done by filling one line of air

holes with the dielectric material. The PBG effect leads to strong in-plane confinement and waveguiding.¹⁸ Consequently, a wider PBG leads to a wider bandwidth. Line defect-based waveguides have been demonstrated for THz wave propagation.^{19,20} When compared with other THz waveguiding approaches like effective media or supporting structure based,^{21–28} PC slab waveguides tend to be robust and do not require additional support structures. Furthermore, the geometric parameters of the slab can be tuned to achieve high bandwidths.²⁹ These expedient features make PC slab waveguides ideal candidates for the design of high-capacity THz range interconnects for the development of THz photonic integrated circuit (TPIC).

Dense integration of THz waveguiding systems requires that the performance does not degrade when features like bends are incorporated into their design. However, in conventional line defect waveguides, radius of curvature must far exceed the wavelength of light to avoid large losses at the corners.³⁰ Sharp bends limit the bandwidth of high transmission restricting practical applications. This loss in bandwidth is also accompanied by bending losses due to scattering at these corners. Significant efforts have been dedicated toward overcoming these limitations. 60° bends were demonstrated by optimizing the shape and size of the air holes of the PC lattice at the corners.³¹ Capsule-shaped defects were introduced which employ total internal reflection (TIR) to bend the waves smoothly around the corners.^{19,32} The bandwidth was still constrained by radiation around the defect causing bending loss. Bends with radius twice the operational wavelength of light equal to 2 mm have also been engineered using the effective media approach.¹⁵ Though standalone Si rectangular/strip waveguides offer an alternative to designing bent waveguiding channels for THz propagation, they are beset by several physical and operational difficulties. Firstly, these waveguides are multimode in nature. Higher-order modes supported by these waveguides could adversely interact with the fundamental mode leading to multimode interference and higher radiative losses.^{33,34} Additionally, such strip waveguides are difficult to handle and require complex support structures. Scattering free transport at bends could also be enabled using intriguing physics of photonic topological insulators where topological protection supports robust waveguiding.^{35–40} However, the bandwidth of such structures is limited and, therefore, renders infeasible the transmission of multiple channels centered at different carrier frequencies. The higher data rates and the co-existence of multiple communication channels in wide bandwidth devices allow for a great degree of freedom in using such devices to develop THz communication systems. Multiple channels sharing the same front-end reduce system complexity. Additionally, due to channel signal-to-noise ratio (SNR) being inversely proportional to transmission channel bandwidth,⁴¹ multicarrier narrow-band channels have key advantages in transmitting signal penalty and data transfer capacity over one single-carrier broadband channel.

In this work, we unveil a sub-wavelength radial bent waveguide platform on a Si PC slab, where the broadband (90 GHz with 25.35% of fractional bandwidth around 355 GHz) nature of device is preserved even in the presence of multiple bends along the waveguiding path. In our design, line defects were created in PC slab for straight waveguiding, while Si rectangular waveguide sections were used to introduce bends of various degrees (90°, 120°, and 180°). Sharp bending radii and scattering at the corners due to the PC slab region are major contributors to the bending losses. We reduce the bending losses through careful design of the bend-region. In conventional line defect

waveguides, light is scattered upon reaching the corners. Typical approaches to reduce bending-induced scattering losses involve engineering the bends by joining adjacent air holes to remove these scattering centers in the bend-region. Our device is a natural extension of such approaches where we join all the air holes on both sides of the rectangular waveguide region to form an air gap region about a quarter-wavelength ($\frac{\lambda}{4}$, where λ is the free space wavelength) on the either side of Si waveguide bend. The sub-wavelength bending radius of these circular rectangular waveguide bends was chosen after taking into consideration the radiation loss and mode distortion of the propagating EM mode. The high bandwidth of the bent waveguide is utilized to support multicarrier transmission by dividing the available bandwidth into four non-overlapping frequency bands centered around different carrier frequencies. We also perform a data communication experiment to transmit four QAM-modulated channels at different carrier frequencies to achieve an aggregate data transfer rate of 327 Gbps. This demonstration opens new avenues for on-chip TPIC waveguide technology and low-loss interconnects and addresses key challenges in achieving high aggregate data rates in compact multicarrier systems for 6G to XG wireless communications.

Figure 1(a) shows the schematic of our broadband Si waveguide system, which comprises of straight PC and the bent rectangular slab waveguiding region. The chip has been made with high resistivity Si (HR-Si) with resistivity >10 k Ω -cm due to low-loss feature of HR-Si at THz frequencies, better refractive index contrast ($n \sim 3.2$), and CMOS integrability. The chip thickness is chosen to be 200 μm to ensure vertical confinement in both the defect and the slab regions. The finite bandgap of the PC defect region determines the operational bandwidth of the device, which supports four independent high-speed communication channels with different carrier frequencies (f_{c1} , f_{c2} , f_{c3} , and f_{c4}). All four channels are well separated in the frequency spectrum to avoid adjacent channel interference. The signal is coupled to the on-chip waveguide through a tapered structure at both ends of the Si slab. The projected image of the PC on the XY plane shown in Fig. 1(b) highlights the PC region, which contains a two-dimensional (2D) triangular lattice of circular air holes with a lattice constant “ a ” of 240 μm and a hole radius “ r ” of $0.3 \cdot a$ (more details in Sec. A of the supplementary material). Filling the air holes in a straight line forms a line defect and enables waveguiding in the PC bandgap region. The rectangular waveguide region, incorporating a bend of 180°, is highlighted (with green color) in Fig. 1(c). The width “ w ” of the rectangular waveguide region is 240 μm , while the optimized bending radius “ r_s ” is 623 μm (bend radius optimization in Sec. B of the supplementary material). The bent region, propagating the entire signal within the PC bandwidth without any significant distortion, is created by removing a circular area of the PC slab with an inner radius “ r_1 ” of 311 μm and an outer radius “ r_2 ” of 935 μm (additional details in Sec. C of the supplementary material). The width “ w ” of waveguiding region, for the lateral confinement of propagating mode, is equal to the lattice constant “ a ,” which is advantageous compared to topological edge state-based waveguides, where lateral confinement along domain wall is spread out to about 5 times the unit cell periodicity.³⁸ The bending radius (r_s) to free space wavelength (“ λ ” corresponding to the central frequency of the PC bandgap) ratio ($\frac{r_s}{\lambda}$) of 0.74 enables sub-wavelength bending radius throughout the device bandwidth. The bending radius is chosen to perfectly align the rectangular waveguide region with the line defect. Figure 1(d) shows the optical image of the fabricated sample. The same bending

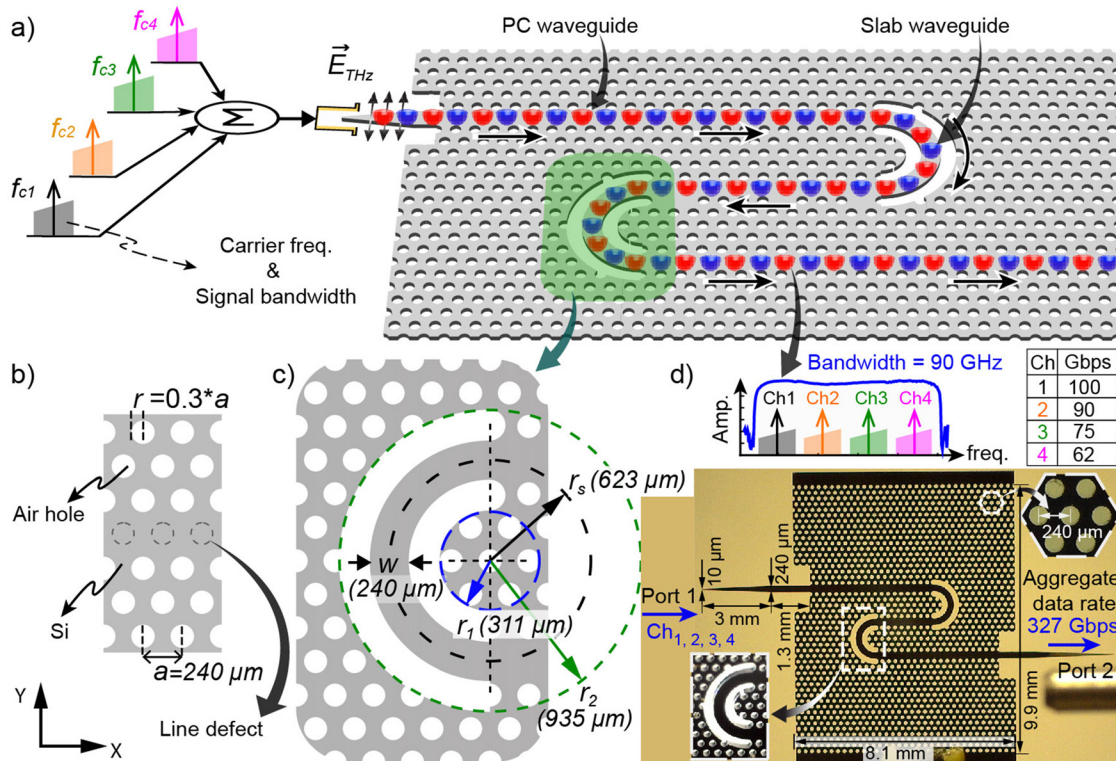


FIG. 1. On-chip hybrid PC-rectangular slab waveguide. (a) Schematic image showing broadband waveguide with bends and supporting four high-speed/broadband channels (Ch1, Ch2, Ch3, and Ch4) centered around carrier frequencies (f_{c1} , f_{c2} , f_{c3} , and f_{c4}). (b) Projection of straight (left) and (c) bent (right) waveguiding region on the XY plane. The straight waveguide is realized by creating a line defect (removing row of air holes as shown by dotted circle) in Si PC slab with drilled air holes of radius " r " with a lattice constant " a " equal to $240 \mu\text{m}$. The bent rectangular waveguide has a width " w " of $240 \mu\text{m}$ and a bending radius " r_s " equal to $623 \mu\text{m}$ with circular air gap region extending to radius " r_1 ($311 \mu\text{m}$)" and " r_2 ($935 \mu\text{m}$)" on either side of the bent region. (d) Optical image of the fabricated sample, where zoomed images at the top right and bottom left show Si PC with air holes and waveguide bends, respectively. The device supports four independent communication channels via Port 1 and Port 2 within the device bandwidth of 90 GHz with an aggregated data rate of 327 Gbps.

strategy is used to realize rectangular waveguide bends of 90° and 120° (sample images in Sec. D of the supplementary material). The bandwidth of fabricated device is sufficient to accommodate spectrally separated four high-speed independent QAM-32 modulated channels (Ch1, Ch2, Ch3, and Ch4) to support an aggregate data transfer rate of 327 Gbps. The surface roughness of the Si slab used for device fabrication may affect the device bandwidth especially if there is a large variation in air holes radius during the Si etching process (more details in Sec. E of the supplementary material).

The advantage of PC in designing the on-chip wideband wave propagation channels could be further understood by the photonic band structure of 2D lattice of air holes in Si slab. The large bandwidth has been made possible by the prudent optimization of the PC lattice parameters. COMSOL Multiphysics based photonic band structure calculation of unit cell for the 2D periodic lattice reveals the existence of a PBG for transverse electric (TE) modes (shown in Sec. A of the supplementary material). A Line defect is created in PC slab for wave propagation, where waveguiding is enabled by the PBG effect contributing to lateral confinement (XY plane) and TIR enabling vertical confinement (z-direction) ¹¹. Figure 2(a) shows the numerically calculated projected band diagram for the PC slab with line defect,

where even (solid blue curve) and odd (dotted blue curve) TE modes are supported in the bandgap region. Compared to odd mode, even mode is broadband, exists in the frequency range from 300 to 390 GHz, and could be excited through hollow rectangular metallic waveguides via tapered Si couplers. Even mode possesses *even* spatial symmetry, as shown by the simulated normalized magnetic field $|H_z|$ distribution, and has linear dispersion for almost 72% of the PBG (~ 65 GHz) region. Though the rectangular waveguides used to incorporate the bends feature higher bandwidths, their fragility necessitates the use of auxiliary support structures, impeding their translation into on-chip THz waveguiding platforms⁴² for TPIC applications. We negate such requirements by using rectangular waveguides only at the bends, where they are supported by the PC slab. Using these two waveguiding systems in tandem ensures lossless propagation of light through multiple tight bends with low bending losses. Figure 2(b) shows the magnetic field profile (H_z) of the propagating modes in all the waveguides with bends and a straight waveguide featuring only a line defect waveguide. The bends transmit the electromagnetic modes between the waveguiding line defects in PC without any significant bending loss and reduction in the transmission channel bandwidth. The measured transmission spectra, in Fig. 2(c), showcase the low-loss

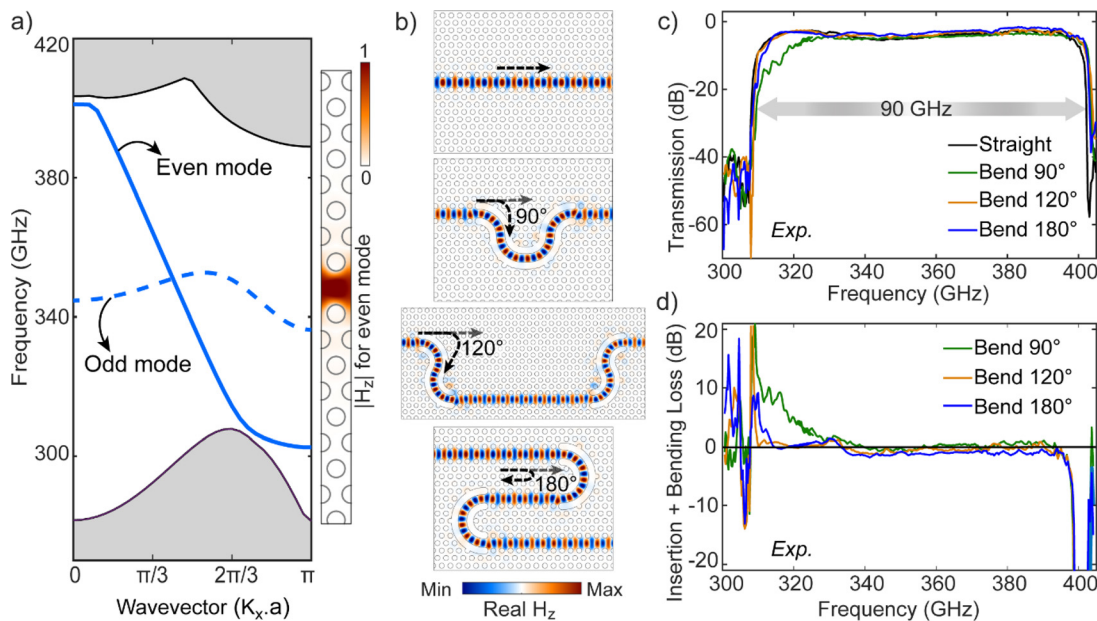


FIG. 2. Broadband all-Si sub-wavelength bend engineered waveguide interconnect for THz photonic integrated circuit (TPIC): (a) Projected band diagram (left image) of periodic line defect PC waveguide, where solid (even mode) and dashed (odd mode) blue lines show the dispersion of the TE modes in the PC bandgap between the bulk bands (grey region). Simulated normalized magnetic field ($|H_z|$) distribution (right image) of the even TE mode, for which the line defect region supports broadband wave propagation. (b) Real component of magnetic field profile (H_z) at 330 GHz for straight, 90° bend, 120° bend, and 180° bend showing good confinement and low-loss propagation at the engineered bends with a bending radius of 0.74λ , where “ λ ” is the free space wavelength corresponding to central frequency of the device bandwidth. (c) Experimentally measured transmission for the four waveguides highlighting the structure’s wide bandwidth (90 GHz). (d) “Insertion + Bending” loss for the bend engineered waveguides as compared to the straight waveguide. The 0 dB black line indicates reference loss line with respect to the straight waveguide.

signal transport performance of the fabricated PC devices with and without bends (measurement method in Sec. F of the supplementary material). Next, we compare the losses in the bent waveguides with that of the straight waveguide. Figure 2(d) shows the total loss, the sum of insertion and bending losses, of all the waveguiding configurations obtained by subtracting the transmission of the straight waveguide from the bent waveguides. However, we observe significant bending loss at lower frequencies in PC devices with 90° bends. The effects of insertion losses, which arise due to misalignment of tapered couplers with the WR 2.8 metallic hollow waveguides, cannot be neglected in low-loss waveguiding platforms. Experimental limitations curtail any attempts to make the insertion losses equal for all samples leading to inconsistent behavior of total loss. Hence, the 180° bend appears to have lower losses compared to the straight waveguide. Furthermore, no significant contribution due to bending losses could be observed in the waveguides with 120° and 180° bend. Better estimates of bending losses can be obtained experimentally using samples with large number of bends where the bending losses will become a major contributor compared to insertion losses. Bending loss for different number of bends was obtained via simulations by setting the insertion losses to be equal. For bent PC waveguides, simulated transmission spectra show that the bending loss is negligible for operational frequencies beyond 340 GHz, but it varies from 1.4 to 1.9 dB in the lower frequency range of the transmission bandwidth (additional information in Sec. G of the supplementary material).

The group delay (GD) of a device enables quantitative estimation of phase distortion in the signal path. Rapid variations or ripples in the group delay are indicative of a dispersive device, which could distort the passing modulated data signal leading to incorrect signal reconstruction at the receiver.⁴³ Therefore, devices are engineered to have flat group delay to ensure low bit error rates (BER) in data transmission. Figure 3(a) shows the experimentally measured group delay within the transmission bandwidth of the PC waveguide with 180° bend (group delay of all samples in Sec. H of the supplementary material). At the center of the transmission bandwidth, the measured group delay for a physical propagation length of 23.76 mm is around 0.3 ns, while at both ends of the bandwidth, the group delay increases nonlinearly. A salient feature of the PC waveguide is the limited phase distortion highlighted by the flat group delay in the transmission bandwidth. Desirable traits like low-loss transmission and flat group delay over a large bandwidth make the PC waveguide a prime candidate to transmit complex IQ-modulated signals. To substantiate this utility of the broadband PC platform, we performed data communication (datacom) experiments by allocating the entire bandwidth to four independent channels (detailed THz communication setup details in Sec. F of the supplementary material). Figure 3(a) also shows the portion of transmission bandwidth allocated to each channel (Ch1: 20 GHz, Ch2: 18 GHz, Ch3: 15 GHz, and Ch4: 12.5 GHz). Sufficient spectral separation between adjacent channels minimizes the risk of channel interference while determining the aggregate data capacity of the on-chip device using the entire available bandwidth. Through each

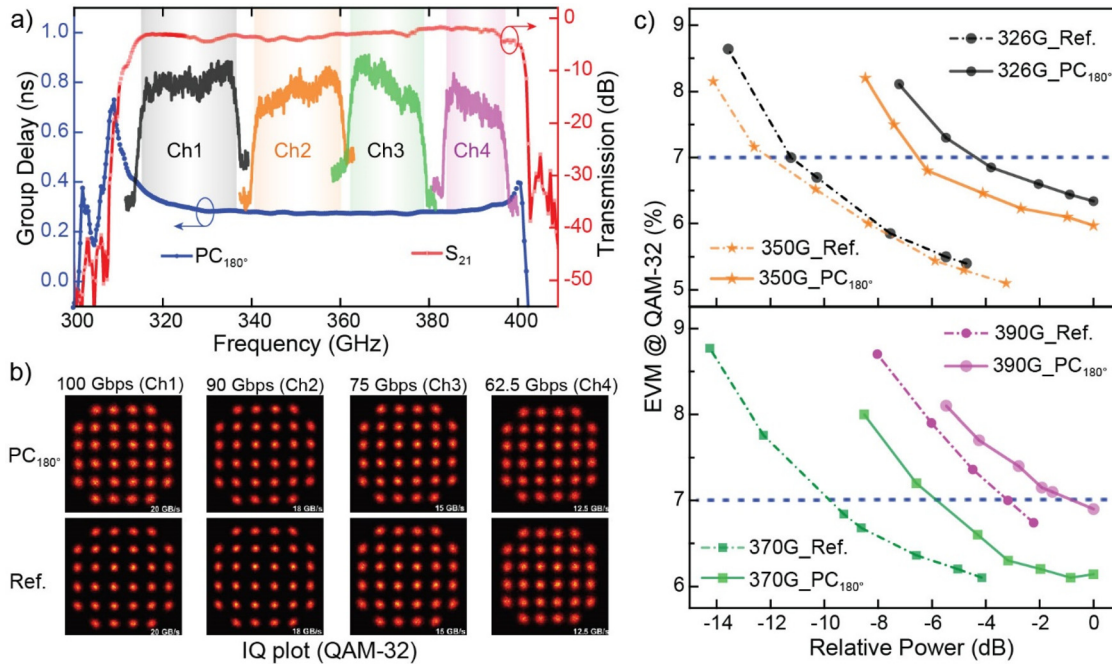


FIG. 3. 327 Gbps on-chip communication with THz waveguide interconnects. (a) Experimentally measured group delay for PC waveguide with 180° bend, and bandwidth of individual channels (Ch1, Ch2, Ch3, and Ch4) within the transmission window of PC waveguide. (b) IQ constellation diagram and data rate (Gbps) for individually transmitted QAM-32 modulated channels with (PC_{180°}) and without (Ref.) bent PC waveguide. (c) EVM @ QAM-32 vs relative power transmitted with (solid line for PC_{180°}) and without (dotted line for Ref.) for Ch1 and Ch2 (top figure), and Ch3 and Ch4 (bottom figure). Top figure corresponds to carrier frequency 326 and 350 GHz, while bottom figure corresponds to carrier frequency 370 and 390 GHz.

channel, QAM-32 modulated data signal with baud rate equal to the channel bandwidth is transmitted to estimate the data capacity. The carrier frequency of each channel is the central frequency of the assigned spectral range of the respective channel. The details of the four communication channels are summarized in Table I. Additionally, using Real Time Oscilloscope (RTO) based setups with 70 GHz bandwidth, we capture the constellation diagrams, and the error vector magnitude (EVM) of the IQ-modulated signal. Figure 3(b) shows the IQ constellation plots for all the channels captured at the receiver after the modulated signal passes through the 180° bend incorporated PC waveguide. These constellation plots are compared with that of the reference (Ref.) constellation plots. However, high frequency RF losses from the RTO setup limit the ability to capture high data transfer capacities at higher carrier frequencies necessitating a trade-off wherein the baud rate is lowered

TABLE I. Communication channel parameters for the data communication experiment using QAM-32 modulation format for all channels.

Channel	Freq. range (GHz)	Carrier freq. (GHz)	Symbol rate (GBaud)	Data rate (Gbps)
Ch1	315–337	326	20	100
Ch2	340–360	350	18	90
Ch3	362–378	370	15	75
Ch4	383–397	390	12.5	62.5

for the higher carrier frequencies to ensure successful detection of the bits in transmitted signal. Furthermore, as shown in Fig. 3(c), we compare the EVM vs relative transmission power for all four channels, to quantify the performance of the 180°-bend PC waveguide as a THz transmission channel. The top figure shows the experimentally measured EVM performance for Ch₁ and Ch₂ with and without PC waveguide, while the bottom figure shows EVM performance for Ch₃ and Ch₄. It is evident that increasing the transmitted power improves the signal-to-noise ratio (SNR), thus reducing the EVM for all data transmitting channels with (PC_{180°}) and without (Ref.) chip.

We estimate the power penalty or the additional transmission power required to overcome the channel losses introduced by the PC waveguide to restore the channel performance at constant EVM to the case without the chip (Ref. case). The power penalty is quite sensitive to the spectral bandwidth of the QAM-32 modulated signal. Reducing the transmitting channel bandwidth from 20 to 12.5 GHz reduces the signal noise, improving the SNR leading to a lower power penalty at the lower baud rate. For a fixed EVM value of 7%, the PC waveguide chip introduces a power penalty of 7, 5.5, 4, and 2 dB for Ch₁, Ch₂, Ch₃, and Ch₄, respectively. Apart from the impact of baud rate on the penalty, the increase in the impact on Ch₁ can also be attributed to the higher group delay dispersion closer to the lower-end of the available bandwidth [Fig. 3(a)]. Furthermore, to highlight the importance of our PC waveguide with sub-wavelength bends, we compared its performance with the recently demonstrated on-chip topological waveguide platform (as shown in Table II).

TABLE II. Performance comparison of our Si slab based sub-wavelength bend PC waveguide with topological waveguide.

Sl. No.	Performance metric	Topological waveguide	Bent PC waveguide (this work)
1	Bandwidth	~ 35 GHz ³⁵	> 90 GHz
2	Propagating mode lateral extent	$\sim 4 \lambda_{Si}$ ^{a,42,44}	$\sim \lambda_{Si}$ ^a
3	Bending angle	60° and 120° ⁴⁵ (Hexagonal lattice)	30°, 60°, 90°, 120°, 180° (Flexible)
4	Back scattering due to bends	Robust to sharp bends	Depends on bending radius
5	Insertion loss in coupling the signal to waveguide. (via tapered Si coupler)	High ^{46–48}	Negligible
6	Data speed using THz as carrier	Up to 160 Gbps ³⁵ (single carrier freq.)	Up to 327 Gbps (multiple carrier freq.)

^a λ_{Si} : Wavelength in Si slab.

In conclusion, broadband waveguide platform with sub-wavelength bends offers a promising solution for densely integrating various sub-wavelength photonics components in emerging THz photonic integrated circuit (TPIC) applications. We experimentally demonstrated an on-chip Si-based defect PC waveguide platform with bends, where ultralow loss transmission of the signal through the chip is observed throughout the device bandwidth. The bending radius, which is nearly 0.74 times the wavelength corresponding to the central frequency (355 GHz) of the device bandwidth, shows nearly identical performance to straight PC waveguide. Building on this, we also perform a communication experiment with four independent non-overlapping channels to utilize the entire device bandwidth and achieve an aggregate data transfer rate of 327 Gbps. Our design strategy will aid the development of THz electronic-photonic integrated circuitry with a reduced footprint and several on-chip functionalities for more reliable, cost-effective, and broader bandwidth terabit per second 6G to XG interconnect and wireless communication applications.

See the supplementary material for bandgap calculations, experimental details, waveguide bend optimization, sample images, and fabrication details.

The authors acknowledge the financial support from the National Research Foundation (NRF), Singapore, under Grant No. NRF-CRP23-2019-0005. G.D. and P.S. acknowledge the support from 'France 2030' programs, PEPR (Programmes et Equipements Prioritaires pour la Recherche), and CPER Wavetech. The PEPR is operated by the Agence Nationale de la Recherche (ANR), under the grants ANR-22-PEEL-0006 (FUNTERA, PEPR 'Electronics') and ANR-22-PEFT-0006 (NF-SYSTEMA, PEPR 5G and beyond – Future Networks). The Contrat de Plan Etat-Region (CPER) WaveTech is supported by the Ministry of Higher Education and Research, the Hauts-de-France Regional council, the Lille European Metropolis (MEL), the Institute of Physics of the French National Centre for Scientific Research (CNRS) and the European Regional Development Fund (ERDF).

AUTHOR DECLARATIONS

Conflict of Interest

The authors have no conflicts to disclose.

Author Contributions

Manoj Gupta: Conceptualization (equal); Data curation (equal); Formal analysis (lead); Investigation (equal); Methodology (equal);

Project administration (equal); Writing – original draft (equal); Writing – review & editing (equal). **Nikhil Navaratna:** Conceptualization (supporting); Data curation (supporting); Formal analysis (supporting); Investigation (equal); Writing – original draft (equal); Writing – review & editing (equal). **Pascal Szriftgiser:** Data curation (supporting); Formal analysis (supporting); Investigation (supporting); Writing – review & editing (supporting). **Guillaume Ducournau:** Data curation (equal); Formal analysis (supporting); Investigation (equal); Methodology (equal); Writing – review & editing (supporting). **Ranjan Singh:** Conceptualization (equal); Funding acquisition (lead); Project administration (equal); Supervision (lead); Writing – original draft (supporting); Writing – review & editing (supporting).

DATA AVAILABILITY

The data that support the findings of this study are available from the corresponding author upon reasonable request.

REFERENCES

- J. C. Balzer, C. J. Saraceno, M. Koch, P. Kaurav, U. R. Pfeiffer, W. Withayachumnankul, T. Kürner, A. Stöhr, M. El-Absi, A. A.-H. Abbas, T. Kaiser, and A. Czulwik, "THz systems exploiting photonics and communications technologies," *IEEE J. Microwave* **3**(1), 268–288 (2023).
- T. Nagatsuma, G. Ducournau, and C. C. Renaud, "Advances in terahertz communications accelerated by photonics," *Nat. Photonics* **10**(6), 371–379 (2016).
- H.-J. Song and T. Nagatsuma, "Present and future of terahertz communications," *IEEE Trans. Terahertz Sci. Technol.* **1**(1), 256–263 (2011).
- J. S. Melinger, S. S. Harsha, N. Laman, and D. Grischkowsky, "Guided-wave terahertz spectroscopy of molecular solids [Invited]," *J. Opt. Soc. Am. B* **26**(9), A79–A89 (2009).
- N. Navaratna, Y. J. Tan, A. Kumar, M. Gupta, and R. Singh, "On-chip topological THz biosensors," *Appl. Phys. Lett.* **123**(3), 033705 (2023).
- M. Beruete and I. Jáuregui-López, "Terahertz sensing based on metasurfaces," *Adv. Opt. Mater.* **8**(3), 1900721 (2020).
- W. L. Chan, J. Deibel, and D. M. Mittleman, "Imaging with terahertz radiation," *Rep. Prog. Phys.* **70**(8), 1325 (2007).
- D. M. Mittleman, "Twenty years of terahertz imaging [Invited]," *Opt. Express* **26**(8), 9417–9431 (2018).
- H. Matsumoto, I. Watanabe, A. Kasamatsu, and Y. Monnai, "Integrated terahertz radar based on leaky-wave coherence tomography," *Nat. Electron.* **3**(2), 122–129 (2020).
- R. Kakimi, M. Fujita, M. Nagai, M. Ashida, and T. Nagatsuma, "Capture of a terahertz wave in a photonic-crystal slab," *Nat. Photonics* **8**(8), 657–663 (2014).
- D. Headland, M. Fujita, G. Carpintero, T. Nagatsuma, and W. Withayachumnankul, "Terahertz integration platforms using substrateless all-silicon microstructures," *APL Photonics* **8**(9), 091101 (2023).

- ¹²R. A. S. D. Koala, M. Fujita, and T. Nagatsuma, "Nanophotonics-inspired all-silicon waveguide platforms for terahertz integrated systems," *Nanophotonics* **11**(9), 1741–1759 (2022).
- ¹⁵N. Margalit, C. Xiang, S. M. Bowers, A. Bjorlin, R. Blum, and J. E. Bowers, "Perspective on the future of silicon photonics and electronics," *Appl. Phys. Lett.* **118**(22), 220501 (2021).
- ¹⁴A. Kumar, M. Gupta, and R. Singh, "Topological integrated circuits for 5G and 6G," *Nat. Electron.* **5**(5), 261–262 (2022).
- ¹⁵A. Kumar, M. Gupta, P. Pitchappa, N. Wang, M. Fujita, and R. Singh, "Terahertz topological photonic integrated circuits for 6G and beyond: A perspective," *J. Appl. Phys.* **132**(14), 140901 (2022).
- ¹⁶A. Scherer, O. Painter, J. Vuckovic, M. Loncar, and T. Yoshie, "Photonic crystals for confining, guiding, and emitting light," *IEEE Trans. Nanotechnol.* **1**(1), 4–11 (2002).
- ¹⁷*Photonic Crystals: Molding the Flow of Light*, 2nd ed., edited by J. D. Joannopoulos (Princeton University Press, Princeton, 2008).
- ¹⁸Y. Sakasegawa, T. Ihara, and K. Hirakawa, "Terahertz photonic band gap for the transverse-magnetic modes formed by using a planar waveguide structure with a photonic crystal electrode," *Appl. Phys. Lett.* **97**(5), 051110 (2010).
- ¹⁹K. Tsuruda, M. Fujita, and T. Nagatsuma, "Extremely low-loss terahertz waveguide based on silicon photonic-crystal slab," *Opt. Express* **23**(25), 31977–31990 (2015).
- ²⁰K. Schmidt and R. Kappeler, "Efficient computation of photonic crystal waveguide modes with dispersive material," *Opt. Express* **18**(7), 7307–7322 (2010).
- ²¹W. Gao, X. Yu, M. Fujita, T. Nagatsuma, C. Fumeaux, and W. Withayachumnankul, "Effective-medium-cladded dielectric waveguides for terahertz waves," *Opt. Express* **27**(26), 38721 (2019).
- ²²W. Gao, W. S. L. Lee, X. Yu, M. Fujita, T. Nagatsuma, C. Fumeaux, and W. Withayachumnankul, "Characteristics of effective-medium-clad dielectric waveguides," *IEEE Trans. Terahertz Sci. Technol.* **11**(1), 28–41 (2021).
- ²³R. Koala, R. Maru, K. Iyoda, L. Yi, M. Fujita, and T. Nagatsuma, "Ultra-low-loss and broadband all-silicon dielectric waveguides for WR-1 band (0.75–1.1 THz) modules," *Photonics* **9**(8), 515 (2022).
- ²⁴E. Akiki, M. Verstuyft, B. Kuyken, B. Walter, M. Faucher, J.-F. Lampin, G. Ducournau, and M. Vanwolleghem, "High-Q THz photonic crystal cavity on a low-loss suspended silicon platform," *IEEE Trans. Terahertz Sci. Technol.* **11**(1), 42–53 (2021).
- ²⁵D. Headland, W. Withayachumnankul, M. Fujita, and T. Nagatsuma, "Gratingless integrated tunneling multiplexer for terahertz waves," *Optica* **8**(5), 621–629 (2021).
- ²⁶S. A. Hosseini Farahabadi, M. Entezami, H. Abouali, H. Amarloo, M. Poudineh, and S. Safavi-Naeini, "Sub-terahertz silicon-based on-chip absorption spectroscopy using thin-film model for biological applications," *Sci. Rep.* **12**(1), 17747 (2022).
- ²⁷N. Ranjkesh, S. Gigoyan, H. Amarloo, M. Basha, and S. Safavi-Naeini, "Broadband single-mode THz suspended silicon-on-glass waveguide," *IEEE Microwave Wireless Compon. Lett.* **28**(3), 185–187 (2018).
- ²⁸M. Verstuyft, E. Akiki, M. Vanwolleghem, G. Ducournau, J.-F. Lampin, B. Walter, F. Bavedila, É. Lebouvier, M. Faucher, and B. Kuyken, "Short bends using curved mirrors in silicon waveguides for terahertz waves," *Opt. Express* **30**(5), 6656–6670 (2022).
- ²⁹L. Shen, Z. Ye, and S. He, "Design of two-dimensional photonic crystals with large absolute band gaps using a genetic algorithm," *Phys. Rev. B* **68**(3), 035109 (2003).
- ³⁰A. Mekis, J. C. Chen, I. Kurland, S. Fan, P. R. Villeneuve, and J. D. Joannopoulos, "High transmission through sharp bends in photonic crystal waveguides," *Phys. Rev. Lett.* **77**(18), 3787–3790 (1996).
- ³¹S. Olivier, H. Benisty, C. Weisbuch, C. J. M. Smith, T. F. Krauss, R. Houdré, and U. Oesterle, "Improved 60 degree bend transmission of submicron-width waveguides defined in two-dimensional photonic crystals," *J. Lightwave Technol.* **20**(7), 1198 (2002).
- ³²B. Miao, C. Chen, S. Shi, J. Murakowski, and D. W. Prather, "High-efficiency broad-band transmission through a double-60° bend in a planar photonic crystal single-line defect waveguide," *IEEE Photonics Technol. Lett.* **16**(11), 2469–2471 (2004).
- ³³C. Li, D. Liu, and D. Dai, "Multimode silicon photonics," *Nanophotonics* **8**(2), 227–247 (2019).
- ³⁴S. Iwamatsu, M. Ali, J. L. Fernández-Estévez, J. Tebart, A. Kumar, S. Makhlof, G. Carpintero, and A. Stöhr, "Ultra-wideband multi-octave planar interconnect for multi-band THz communications," *J. Infrared Milli Terahertz Waves* **44**(7), 532–550 (2023).
- ³⁵A. Kumar, M. Gupta, P. Pitchappa, N. Wang, P. Szriftgiser, G. Ducournau, and R. Singh, "Phototunable chip-scale topological photonics: 160 Gbps waveguide and demultiplexer for THz 6G communication," *Nat. Commun.* **13**(1), 5404 (2022).
- ³⁶Y. J. Tan, W. Wang, A. Kumar, and R. Singh, "Interfacial topological photonics: Broadband silicon waveguides for THz 6G communication and beyond," *Opt. Express* **30**(18), 33035–33047 (2022).
- ³⁷M. T. A. Khan, H. Li, N. N. M. Duong, A. Blanco-Redondo, and S. Atakaramians, in *2021 46th International Conference on Infrared, Millimeter and Terahertz Waves* (IEEE, 2021), pp. 1–2.
- ³⁸S. Iwamoto, Y. Ota, and Y. Arakawa, "Recent progress in topological waveguides and nanocavities in a semiconductor photonic crystal platform [Invited]," *Opt. Mater. Express* **11**(2), 319–337 (2021).
- ³⁹W. Sui, Y. Zhang, Z. Zhang, H. Zhang, Z. Lv, Q. Shi, D. Zhang, and B. Yang, "Unidirectional propagation of helical edge states via exciting pseudospin d states in two-dimensional photonic crystals," *Appl. Phys. Lett.* **122**(11), 111103 (2023).
- ⁴⁰K. M. Devi, S. Jana, and D. R. Chowdhury, "Topological edge states in an all-dielectric terahertz photonic crystal," *Opt. Mater. Express* **11**(8), 2445–2458 (2021).
- ⁴¹K. Szczerba, P. Westbergh, E. Agrell, M. Karlsson, P. A. Andrekson, and A. Larsson, "Comparison of intersymbol interference power penalties for OOK and 4-PAM in short-range optical links," *J. Lightwave Technol.* **31**(22), 3525–3534 (2013).
- ⁴²A. Malekabadi, S. A. Charlebois, D. Deslandes, and F. Boone, "High-resistivity silicon dielectric ribbon waveguide for single-mode low-loss propagation at F/G-bands," *IEEE Trans. Terahertz Sci. Technol.* **4**(4), 447–453 (2014).
- ⁴³J. Webber, Y. Yamagami, G. Ducournau, P. Szriftgiser, K. Iyoda, M. Fujita, T. Nagatsuma, and R. Singh, "Terahertz band communications with topological valley photonic crystal waveguide," *J. Lightwave Technol.* **39**(24), 7609–7620 (2021).
- ⁴⁴Q. Zhang, D. Lee, L. Zheng, X. Ma, S. I. Meyer, L. He, H. Ye, Z. Gong, B. Zhen, K. Lai, and A. T. C. Johnson, "Gigahertz topological valley Hall effect in nanoelectromechanical phononic crystals," *Nat. Electron.* **5**(3), 157–163 (2022).
- ⁴⁵Y. Yang, Y. Yamagami, X. Yu, P. Pitchappa, J. Webber, B. Zhang, M. Fujita, T. Nagatsuma, and R. Singh, "Terahertz topological photonics for on-chip communication," *Nat. Photonics* **14**(7), 446–451 (2020).
- ⁴⁶C. A. Rosiek, G. Arregui, A. Vladimirova, M. Albrechtsen, B. Vosoughi Lahijani, R. E. Christiansen, and S. Stobbe, "Observation of strong backscattering in valley-Hall photonic topological interface modes," *Nat. Photonics* **17**(5), 386–392 (2023).
- ⁴⁷M. Gupta, A. Kumar, and R. Singh, "Electrically tunable topological notch filter for THz integrated photonics," *Adv. Opt. Mater.* (to be published 2023).
- ⁴⁸L. Chen, M. Zhao, H. Ye, Z. H. Hang, Y. Li, and Z. Cao, "Efficient light coupling between conventional silicon photonic waveguides and quantum valley-Hall topological interfaces," *Opt. Express* **30**(2), 2517–2527 (2022).